Laser-Induced Ocular Hypertension in Albino CD-1 Mice

Christine T. Fu[1,2,3] *and David Sretavan*[1,2,3]

Purpose. To establish a laser-induced model of ocular hypertension (LIOH) in albino CD-1 mice and to characterize the sequence of pathologic events triggered by intraocular pressure (IOP) elevation.

Methods. LIOH was induced unilaterally in CD-1 mice by laser photocoagulation of limbal and episcleral veins 270° to 300° circumferentially, sparing the nasal aspect and the long ciliary arteries. IOP was measured with a rebound tonometer. Hematoxylin and eosin-stained plastic sections were used for morphometric analysis of retinal layers, and retinal whole-mounts were immunostained with anti-Brn-3b to quantify retinal ganglion cell (RGC) gene expression ion and density. Axonal and myelin morphologies were characterized using appropriate antibodies, and axon counts were obtained from paraphenylenediamine-stained optic nerve sections.

Results. LIOH resulted in IOP doubling within 4 hours after laser treatment, which returned to normal by 7 days. Axon degenerative changes, reactive plasticity, and aberrant regrowth were detected at the optic nerve head (ONH) as early as 4 days after treatment. By 7 days, axon number was significantly reduced in the myelinated optic nerve, with concurrent signs of myelin degradation. At 14 days, Brn-3b$^+$ RGC density was reduced, with neuronal loss confined to the RGC layer and no apparent effects on other retinal layers.

Conclusions. Laser photocoagulation of limbal and episcleral veins induces transient ocular hypertension in albino CD-1 mice. The ensuing retinal and optic nerve pathologic events recapitulated key features of glaucoma and placed ONH RGC axon responses as an early manifestation of damage. LIOH in albino mice may be useful as a mouse model to examine mechanisms of RGC and axon glaucomatous injury. (*Invest Ophthalmol Vis Sci.* 2010;51:980–990) DOI:10.1167/iovs.09-4324

Animal models of glaucoma are important tools for elucidating pathogenic mechanisms and for testing potential therapeutic modalities.[1–5] Each model system has unique strengths and limitations. Nonhuman primate eyes are anatomically most similar to human eyes, yet experimentation with monkeys is limited by its high cost and is not well suited for studies requiring large numbers of animals. Among rodent models commonly used in glaucoma research, mouse models offer the distinct advantage of enabling genetic manipulation. Although DBA/2J is the best-characterized mouse model of glaucoma,[6] the penetrance of glaucomatous damage is incomplete, and the onset of disease in individual animals cannot be precisely defined. Furthermore, the analysis of gene function requires extensive breeding of mutant alleles into the inbred DBA/2J background. In this study, we sought to develop and characterize a laser-induced experimental model in CD-1 mice based on several rationales. First, CD-1 is an albino outbred stock whose genetic heterogeneity more closely mimics the variability of human population than do inbred strains.[7] Second, because of superior breeding performance, CD-1 is widely used by investigators to maintain mutant mouse strains. The addition of a CD-1 model to the repertoire of available glaucoma models would, therefore, facilitate the genetic analysis of this complex disease. Third, although laser photocoagulation has previously been described in pigmented mice,[8–11] there are no published reports of such work in albino mice. Given that the absence of melanin dramatically alters the absorption of laser energy by ocular tissues, a distinct set of operative parameters must be established for the successful induction of glaucoma. Fourth, the lack of pigmentation in CD-1 mice facilitates visualization of ocular vasculature, thus enabling better targeting of laser power.

Here we describe our studies of the induction of ocular hypertension in CD-1 mice using laser photocoagulation of limbal and episcleral veins. Major pathologic responses in this model consisted of retinal ganglion cell (RGC) axon damage and the loss of RGC molecular markers in cell somas, similar to findings in DBA/2J glaucomatous mice. Using the precise onset of ocular hypertension in this laser model, we placed these key pathologic events in an approximate temporal sequence. The earliest detectable morphologic sign of damaged occurred in RGC axons at the optic nerve head (ONH) and included both degenerative changes and a previously undocumented phenomenon of axon reactive plasticity and aberrant growth.

Materials and Methods

Animals

CD-1 mice were purchased from Charles River Laboratories (Wilmington, MA) and were housed in animal facilities at the University of California, San Francisco (UCSF). Mice 3 to 6 months of age were used for the measurement of IOP profile (see Fig. 1). No significant difference was noted between 3- and 6-month-old mice within this group. Subsequent experiments (see Figs. 2–7) were conducted in animals 3 to 4 months of age. All experiments were performed according to protocols approved by the UCSF Institutional Animal Care and Use Committee and in accordance with the ARVO Statement for the Use of Animals in Ophthalmic and Vision Research.

Laser-Induced Ocular Hypertension

Adult albino CD-1 mice were anesthetized with intraperitoneal injections of 90 mg/kg ketamine HCl and 6 mg/kg xylazine. After loss of the toe pinch reflex, mice were placed on the platform of a slit lamp biomicroscope equipped with a diode laser (532 nm; Lumenis, Santa

From the [1]Neuroscience Graduate Program and the Departments of [2]Ophthalmology and [3]Physiology, University of California, San Francisco, San Francisco, California.

Supported by the National Eye Institute Grants EY016688 and EY02162, Research to Prevent Blindness, and That Man May See Foundation. DS is the recipient of a Research to Prevent Blindness Senior Scientific Investigator Award.

Submitted for publication July 16, 2009; revised August 17, 2009; accepted September 22, 2009.

Disclosure: **C.T. Fu**, None; **D. Sretavan**, None

Corresponding author: Christine T. Fu, Department of Ophthalmology, University of California, San Francisco, Box 0730, 10 Koret Way, San Francisco, CA 94143; cfu@vision.ucsf.edu.

Clara, CA). Photocoagulation of limbal and three episcleral veins was induced unilaterally (150-mW laser power, 0.2-second duration, 100-μm diameter spot size) to obstruct aqueous outflow. The translimbal laser treatment was performed over 270° to 300°, sparing the nasal aspect and the long posterior ciliary arteries. Avoiding the long posterior ciliary arteries greatly reduced ocular inflammation after laser surgery, and the lack of pigmentation in CD-1 was advantageous in facilitating identification of these arteries. Laser spots were applied around these vessels that supply the iris from both the nasal and the temporal poles, resulting in one major laser-free zone nasally and one minor laser-free zone temporally. Both eyes were kept moist with saline at all times. After surgery, bacitracin antibiotic ointment was administered to the operative eye. Each animal received only one round of laser photocoagulation treatment. The contralateral eye was untreated and served as the control.

IOP Measurement

Mice anesthetized with 90 mg/kg ketamine HCl and 6 mg/kg xylazine were placed on an adjustable-height platform, and IOP in both eyes was measured with a rebound tonometer (TonoLab; Colonial Medical Supply, Franconia, NH) mounted on a ring stand. The probe was triggered with a custom-fitted foot pedal to minimize movement of the instrument body. To control for the diurnal variation in IOP, all measurements were taken between 10 am and noon, as soon as loss of the righting reflex was observed, to avoid the IOP-depressing effect of anesthesia.[12]

After laser treatment, only eyes with IOP elevations greater than 21 mm Hg were used in subsequent analysis. Although there is no accepted threshold value of IOP in mice beyond which is indicative of glaucoma, we used the value of 21 mm Hg to gauge the success of inducing ocular hypertension after the defined laser experimental protocol. Mice with overt signs of ocular inflammation were euthanatized and excluded from the study.

Retinal Histology and Morphometry

Each mouse was anesthetized with an overdose of pentobarbital and was perfused transcardially with 2% paraformaldehyde (PFA) and 2.5% glutaraldehyde in 0.1 M phosphate-buffered saline (PBS; pH 7.4). Eyes were enucleated along with retrobulbar segment of the optic nerve. After removal of the anterior segment, lens, and vitreous, eyecups consisting of retina and optic nerve were immersion-fixed in the same fixative at 4°C overnight. Samples were embedded in plastic (JB-4; Electron Microscopy Sciences, Hatfield, PA), sectioned at 2 μm, and stained with hematoxylin-eosin. Only sagittal sections through the central ONH were selected to ensure analysis of comparable retinal planes in each sample. Images were collected using an upright microscope (Eclipse E800; Nikon, Tokyo, Japan) equipped with charge-coupled device camera (SPOT; Diagnostic Instruments, Sterling Heights, MI). Measurements of retinal layer thickness were taken from the central (250 μm from the ONH), middle (750–1000 μm from the ONH), and peripheral (100 μm from the ora serrata) retina. Nuclei in the ganglion cell layer (GCL) were counted in 500-μm segments across the central, middle, and peripheral retinal locations, as defined, and were expressed as cells per millimeter to obtain the cell density in the linear dimension along the GCL. One tissue section was analyzed from each of the 10 pairs of control and laser-treated retinas. All measurements were made from both sides of the ONH and were averaged.

PPD Staining and Axon Counting

Mice were perfused with 2% PFA and 2.5% glutaraldehyde fixative. Paraphenylenediamine staining (PPD) was performed, as previously described.[13] Briefly, optic nerves were dissected from 1 mm behind the globe and were postfixed in 2% PFA and 2.5% glutaraldehyde at 4°C. Treatment with 1% OsO_4 in PBS for 2 hours at room temperature was followed by three 10-minute washes with 0.1 M sodium acetate buffer. Tissues were then stained with 2% uranyl acetate in sodium acetate buffer for 1 hour at room temperature, washed in buffer, dehydrated in a graded ethanol series (40%–100%), and infiltrated with propylene oxide-812 resin (1005 Embed 812; EMS, Fort Washington, PA). The samples were embedded with fresh 100% 812 resin in molds and polymerized in a 60°C oven for 36 hours. Sections of 1 μm in thickness were cut and stained with 1% PPD in 1:1 methanol/isopropanol for 30 minutes, washed in fresh isopropanol twice, and coverslipped. The axon counting protocol was based on a published method with modifications.[14] Sections were first imaged under the 20 × objective lens on an inverted microscope (TE300; Nikon), and the optic nerve cross-sectional areas were traced and calculated. Nonoverlapping fields spanning the entire section were then captured with the 100 × lens. The images were collected into a layered graphics editing file (Photoshop; Adobe, Mountain View, CA), and a 20 × 15-μm box was randomly placed on the topmost image. The software then cropped out the same region in all stacked layers, including those invisible to the operator, so as to remove any possibility of inadvertent bias. Manually counted axon numbers in these rectangular boxes were used to calculate axon densities, which were then averaged and multiplied by the cross-sectional area to obtain total axon count.

Cryostat Section Preparation

Animals were perfused transcardially with 4% PFA in 0.1 M PBS (pH 7.4). Eyes were dissected as described, postfixed in 4% PFA at 4°C overnight, and cryoprotected with 30% sucrose. Eyecups were then embedded in optimal cutting temperature (OCT) compound (Tissue-Tek; Sakura Finetek, Torrance, CA), and 10-μm cryosections were cut along the longitudinal axis through the ONH. Sections were mounted on slides (Super Frost Plus; Fisher Scientific, Springfield, NJ) and subjected to immunostaining.

Immunohistochemistry

Cryosections were air-dried at room temperature for 1 hour and were washed with 0.1 M PBS, which also served as a diluent for all subsequent reagents. Nonspecific binding was blocked with 10% normal donkey serum (NDS) for 30 minutes at room temperature. For most experiments, tissue permeabilization was achieved by inclusion of 0.1% Triton X-100 in the blocking solution. Primary antibodies were diluted in 1% normal donkey serum and incubated with the slides overnight at 4°C. After three PBS washes of 10 minutes each, secondary antibodies were applied for 1 hour at room temperature. Slides were then washed in PBS, counterstained with 4′,6-diamidino-2-phenylindole (DAPI) to label nuclei when appropriate, and mounted in 97% 2,2′-thiodiethanol (TDE; Sigma, St. Louis, MO).

The following primary antibodies were used: rabbit anti-tubulin β-III (1:500; Sigma), mouse anti-neurofilament (SMI312; 1:500; Covance Research Products, Denver, PA), goat anti-Brn-3b (1:50; Santa Cruz Biotechnology, Santa Cruz, CA), mouse anti-2′,3′-cyclic nucleotide 3′-phosphodiesterase (CNPase; 1:500; Sigma, St. Louis, MO), and rabbit anti-degraded myelin basic protein (dMBP; 1:1000; Chemicon, Temecula, CA). Multicolor labeling was accomplished with secondary antibodies conjugated to tetramethyl rhodamine (TMR; 1:200; Invitrogen, Carlsbad, CA) or cy3, cy2, and cy5 (1:200; Jackson ImmunoResearch, West Grove, PA).

Confocal Microscopy

Fluorescence imaging was performed on an inverted confocal laser microscope (LSM5 Pascal; Carl Zeiss Meditec, Inc., Thornwood, NY), using a 20 × air, 63 × oil, or 100 × oil objective. For triple-labeling experiments, images were scanned with the 488-nm, 543-nm, and 633-nm lasers to excite cy2, TMR/cy3, and cy5, respectively. Except when goat primary antibodies were used, TMR was chosen in lieu of cy3 because of its lower excitation by the 488-nm laser, thus minimizing potential bleed-through into the green channel. Scans of different fluorescent channels were collected sequentially, and laser power as well as detector gain were adjusted to eliminate bleed-through between channels.

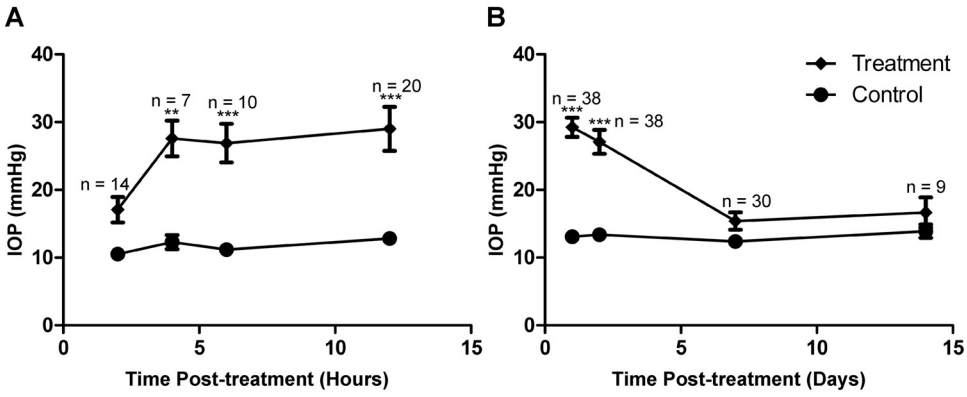

FIGURE 1. Laser treatment induced IOP elevation in CD-1 mice. (**A**, **B**) IOP measurements within 12 hours (**A**) and over 2 weeks (**B**) after treatment. IOP significantly increased in laser-treated eyes between 4 hours and 2 days compared with contralateral control eyes. $^{**}P < 0.01$; $^{***}P < 0.001$.

Retinal Whole-Mount

The retinal whole-mount protocol was modified from a published study.[15] Mice were perfused transcardially, and eyes were harvested as described. The anterior segment, lens, and optic nerve were dissected away, and the retinas were gently freed from the sclera. Care was taken to make sure a short stump of optic nerve (~100 μm) remained attached. Vitreous was removed with a pair of fine forceps. Four radial cuts were made on the retina, which was then flattened onto a small piece of Millipore (Billerica, MA) filter paper. After postfixation in 4% PFA for 30 minutes to 1 hour, the retinas were rinsed in PBS and permeabilized with 0.3% Triton X-100 in PBS for 30 minutes. Nonspecific binding was blocked with 10% NDS in PBS containing 0.1% Tween-20 (PBST) for 30 minutes at room temperature. Primary antibody incubation was performed in PBST with 3% NDS at 4°C overnight. Retinas were washed in PBST three times for 15 minutes each and were incubated with secondary antibodies for 1 hour at room temperature. After gradual equilibration with successively higher concentration of TDE to minimize tissue distortion, samples were mounted in 97% TDE and coverslipped. This mounting medium has the advantage of matching the refractive index of immersion oil, which minimizes spherical aberration when imaging deep into the specimen with confocal microscopy.

To analyze the morphology of pre-lamina ONH, retinal whole-mounts were scanned with a confocal microscope (LSM5 Pascal; Zeiss) starting from the nerve fiber layer, and consecutive optical sections were taken at intervals of 0.5 μm, extending 10 to 20 μm deep into the ONH. Images were reconstructed as compressed *z*-stacks. To estimate the density of Brn-3b$^+$ RGCs, three random fields of 0.2 mm^2 were imaged at central, middle, and peripheral locations in each retina. Confocal *z*-stacks were taken and compressed to account for potential irregularities in the specimen. Labeled RGC nuclei in all 12 fields were counted with ImageJ software (developed by Wayne Rasband, National Institutes of Health, Bethesda, MD; available at http://rsb.info.nih.gov/ij/index.html) and were then averaged.

Experimental Controls

At least three pairs of eyes or ONHs were examined for every antibody marker (summarized as *n* in figure legends). From each sample, at least three tissue sections were analyzed. In experiments comparing signal intensity between different treatment groups, all samples were processed in parallel and were imaged under identical microscope settings. Experiments in which the primary antibody was omitted served as negative controls.

Statistical Analysis

IOP measurements and retinal morphometry data were analyzed by two-way ANOVA. Where a significant main effect was found, the post hoc Bonferroni multiple comparison test was conducted. RGC cell count and axon count data were subjected to one-way ANOVA followed by Tukey's multiple comparison test. Statistical tests were performed using a statistical software (Prism, version 5; GraphPad, San Diego, CA), with a significance level set at $P < 0.05$. Values were reported as mean ± SEM.

RESULTS

IOP Elevation in CD-1 Mice after Laser Treatment

In this study, we sought to develop an experimental model of laser-induced ocular hypertension in CD-1 mice. After laser photocoagulation of limbal and episcleral veins of the aqueous humor outflow pathway in CD-1 mice, IOP was measured at various time points in the operative eye and in the contralateral eye, which did not receive laser treatment and served as control. To rule out transient IOP spikes immediately after laser treatment, which could cause global retinal ischemia, we measured short-term IOP changes within the first 12 postoperative hours (Fig. 1A). In a separate group of mice, we characterized the profile of IOP elevation longitudinally by measuring IOP values at 1 day, 2 days, 1 week, and 2 weeks after treatment (Fig. 1B). Beginning as soon as 4 hours after laser treatment, the IOPs measured in operative eyes (27.6 ± 2.6 mm Hg; $n = 7$) were significantly elevated above those measured in control eyes (12.3 ± 1.0 mm Hg; $n = 7$) and remained elevated at the second postoperative day (operative 27.1 ± 1.8 mm Hg vs. control 13.4 ± 0.3 mm Hg; $n = 38$). IOPs measured in laser-treated eyes declined to baseline and were similar to IOPs in control eyes by 1 week (operative 15.4 ± 1.3 mm Hg vs. 12.4 ± 0.6 mm Hg; $n = 30$). The peak IOP measured immediately after laser treatment (29.2 ± 1.4 mm Hg; $n = 38$) and during the first postoperative week was sufficiently below the mean blood pressure (MBP) of 102 ± 4 mm Hg reported for CD-1 mice.[16] Based on the formula that ocular perfusion pressure equals MBP minus IOP,[17] an eye with a 30 mm Hg IOP maintains approximately 70 mm Hg perfusion pressure, which is unlikely to result in global retinal ischemia. Histologic analysis of retinal sections from laser-treated eyes (Fig. 2) also revealed well-preserved tissue cytoarchitecture except in the ganglion cell and nerve fiber layers, consistent with the maintenance of normal retinal perfusion after laser treatment.

In addition to the cohort of mice used specifically for longitudinal analysis of the IOP profile, the present study consisted of 380 laser-treated mice whose IOPs were recorded 12 to 24 hours after treatment. Of these, 308 (81%) had IOPs ≥ 21 mm Hg and were used in subsequent analysis; 59 (16%) did not meet the 21 mm Hg criterion. A small number (3%) exhibited signs of surgical complication, including hyphema or corneal edema, and were excluded from the study. In our experience with laser-induced ocular hypertension in CD-1 mice, we never observed cataract or phthisis reported for pigmented mice.[9]

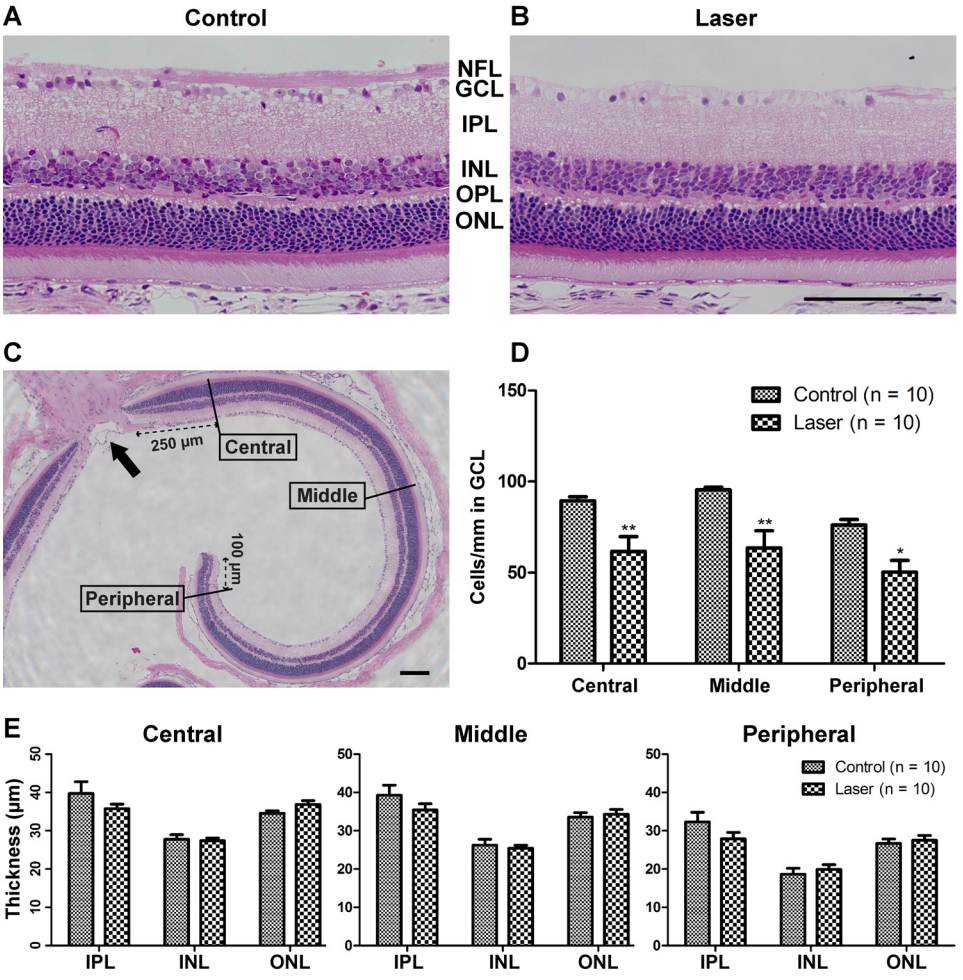

FIGURE 2. Retinal histology and morphometric analysis 4 weeks after laser treatment. (**A**, **B**) Representative images of plastic-embedded, hematoxylin and eosin-stained retinal sagittal section, captured 250 μm from the ONH. The GCL in laser-treated eye (**B**) was greatly reduced in cell number compared with control (**A**). Apparent thinning also occurred in NFL-containing RGC axons. The other retinal layers appeared relatively intact. (**C**) Definition of central (250 μm from the ONH), middle (750–1000 μm from the ONH), and peripheral (100 μm from the ora serrata edge) retinal locations. Note that only midsagittal sections through the ONH (*arrow*) were selected for analysis. (**D**) Linear density of GCL cells expressed as cells per millimeter was significantly reduced at all retinal locations after laser treatment. (**E**) The thickness of IPL, INL, and ONL were not significantly impacted. OPL, outer plexiform layer. Scale bar, 100 μm. $n = 10$ retinas for both control and laser groups. $^{*}P < 0.05$; $^{**}P < 0.01$.

Induced Cell Loss Specific to the Retinal Ganglion Cell Layer

The hallmark of glaucomatous damage is the loss of retinal ganglion cells, with relative sparing of other retinal layers. Retinal histology 4 weeks after laser treatment demonstrated prominent cell loss in the GCL and diminution of the nerve fiber layer (NFL) (compare Figs. 2A and 2B). The other retinal layers were not significantly changed in thickness. To quantify the pattern of damage at different retinal eccentricities, we performed morphometric analysis at central, middle, and peripheral locations on hematoxylin and eosin-stained plastic sections ($n = 10$ for both control and laser-treated retinas). The protocol for defining these regions is illustrated in Figure 2C. Linear density of cells in the GCL was reduced in the central (by 31%), middle (by 33%), and peripheral (by 34%) regions (Fig. 2D). In contrast, the thickness measurements of the inner nuclear layer (INL) and outer nuclear layer (ONL) were not significantly altered at any retinal eccentricity (Fig. 2E). It is worth noting that we observed visible thinning of the inner plexiform layer (IPL) in some laser-treated samples, consistent with the loss of RGC dendritic arbors. Although the mean IPL thickness values in experimental animals were reduced by 10%, 10%, and 14% for the central, middle, and peripheral retina, respectively, this was not a consistent finding and did not reach statistical significance. Overall, the pattern of retinal damage in CD-1 LIOH was consistent with the selective degeneration of RGCs, similar to that which occurs in glaucoma.

In addition to histologic analysis, immunolabeling was used to enable direct quantification of RGC density. Approximately 40% to 60% of cells in the mouse GCL are estimated to be displaced amacrine cells.[18–21] Although we did not directly quantify the survival of amacrine cells, no reduction was found in the thickness of the INL, 40% of which is composed of amacrine cells.[19] This observation would argue that amacrine cells are not vulnerable in LIOH, consistent with previous reports in other rodent models of glaucoma.[22,23] Considering the existence of displaced amacrine cells, the total number of nuclei in GCL does not provide an accurate measure of RGC survival after laser treatment. To overcome this limitation, Brn-3b antibody was used to specifically label RGCs in retinal whole-mounts (Fig. 3). Brn-3b is a transcription factor expressed in a subset of RGCs[15,24] distributed uniformly across the retina, allowing for direct visualization and convenient RGC counting in immunostained retinal whole-mounts. Because previous studies demonstrated that no specific class of RGCs is selectively impacted in mouse glaucoma,[22] we used the density of Brn-3b^{+} nuclei as a surrogate measure of the overall density of surviving RGC somas. The results showed that Brn-3b^{+} RGC density at 1 week after laser treatment was not significantly different from that of control (Fig. 3F). However, there was a substantial (42%) loss of Brn-3b^{+} RGCs compared with control retinas by 2 weeks after laser treatment. By 4 weeks, the average density of Brn-3b^{+} RGCs in laser-treated eyes was reduced by 91% of controls. Thus the loss of Brn-3b expression appeared to commence, on average, between 1 to 2 weeks after laser treatment. Although it is possible that the loss of Brn-3b protein by itself may not mark the death of RGCs, histologic evidence of reduced cell num-

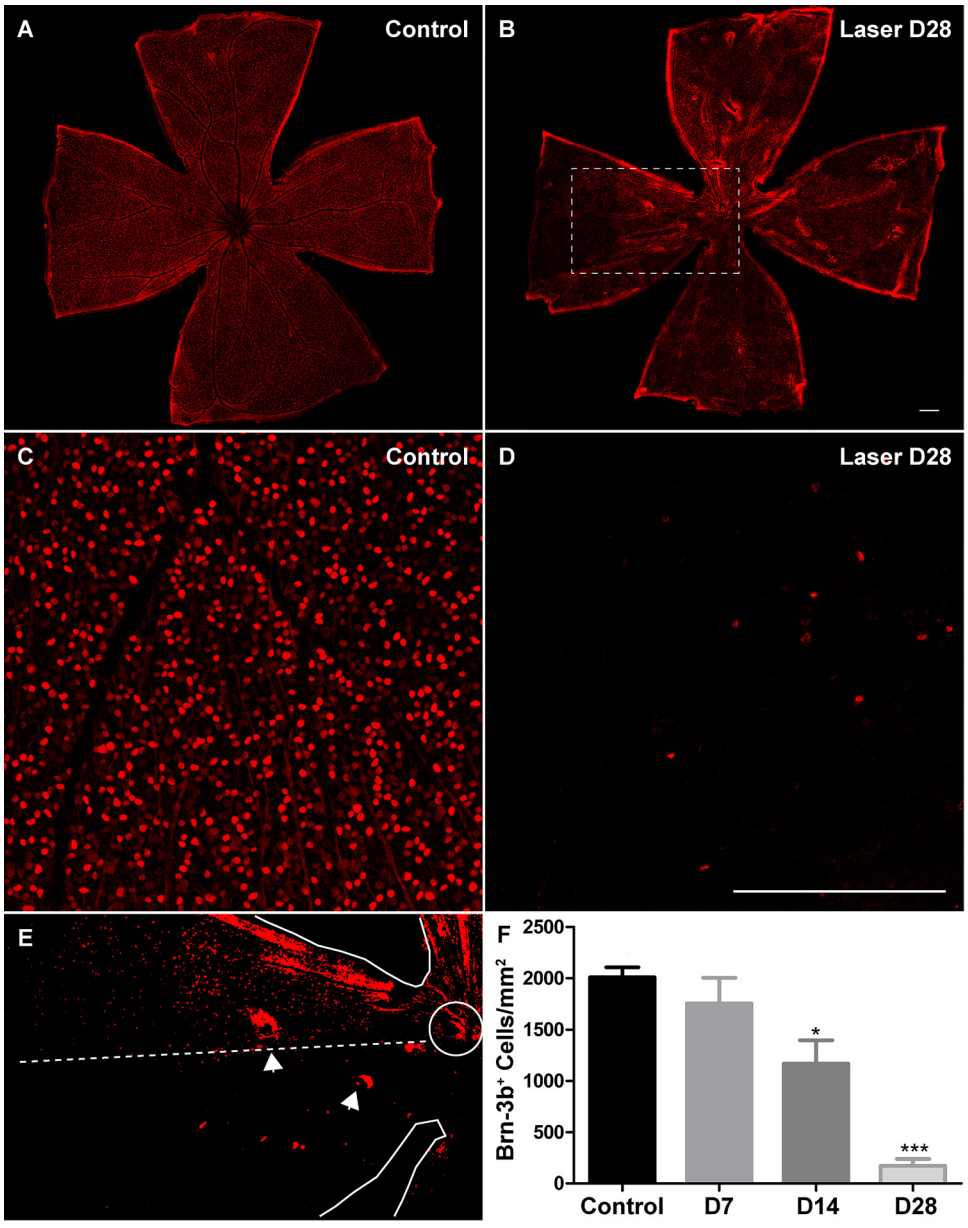

FIGURE 3. Laser treatment resulted in a decrease in the number of Brn-3b$^+$ RGCs in the retina. (**A**, **B**) Low-magnification views of whole-mounted retinas immunolabeled with the Brn-3b antibody. (**C**, **D**) Representative images used for quantification of Brn-3b$^+$ RGC number. (**E**) Higher magnification, binarized image of boxed region in (**B**), highlighting the fan-shaped pattern of Brn-3b$^+$ RGC loss. *Solid traces*: edges of the retinal whole-mount and the ONH. *Dashed line*: imaginary boundary dividing a sector of relative preservation (*above*) from a sector of severe loss (*below*) of Brn-3b$^+$ cells. *Arrowheads*: occasional tearing of the tissue preparation. (**F**) The mean density of Brn-3b$^+$ RGCs in experimental retinas at 2 weeks was reduced by 42% of that in contralateral control eyes and at 4 weeks by 91% of that in control eyes. Scale bar, 200 μm. For each group, eight retinas were analyzed. $^*P < 0.05$; $^{***}P < 0.001$.

bers in the GCL and diminution of the NFL (Fig. 2B) indicates that death does occur in at least a proportion of RGCs (see Discussion). In addition, DAPI staining of experimental retinal whole-mounts revealed substantial reductions in cell number (CTF, DS, unpublished observation, 2008), suggesting that changes in Brn-3b immunolabeling mirrored the overall pattern of RGC degeneration. Furthermore, the loss of Brn-3b$^+$ RGCs was nonuniform across the retina and often appeared sectorial in nature (Fig. 3E). This pattern of RGC damage in laser-treated CD-1 mice is similar to what has been observed in DBA/2J animals using RGC-specific ROSA3 βGeo reporter or retrograde labeling[22,25,26] and is consistent with an insult to discrete axon bundles at the ONH.

Axon Degeneration in the Myelinated Optic Nerve

Recent evidence demonstrated that the degeneration of RGC somas and axons in glaucoma may involve distinct processes.[14] To obtain an independent measure of RGC axon survival, we used PPD to visualize axons in the myelinated optic nerve. PPD is a dye that uniformly labels myelin sheaths but differentially stains the axoplasm of degenerating axons darkly.[14] Figure 4A–D shows examples of PPD-stained optic nerve cross-sections harvested at different time points after laser treatment. In addition to axon degeneration indicated by darkly stained axoplasm or myelin debris (arrowheads), axon swelling (arrows) and gliosis (double arrows) were apparent in experimental nerves. Axon counting revealed that the total axon number was reduced by 47% at 1 week, 68% at 2 weeks, and 78% at 4 weeks. These data agreed with our previous findings focused on RGC somas and confirmed that both RGC axons and somas were damaged after LIOH.

Axon Integrity in the Lamina and Pre-Lamina ONH

One major limitation of inbred mice with spontaneous glaucoma is the undefined onset of disease hindering the study of early disease processes. Using experimental LIOH, we took advantage of the investigator-controlled onset of IOP elevation to examine changes occurring early in disease. Given that RGC

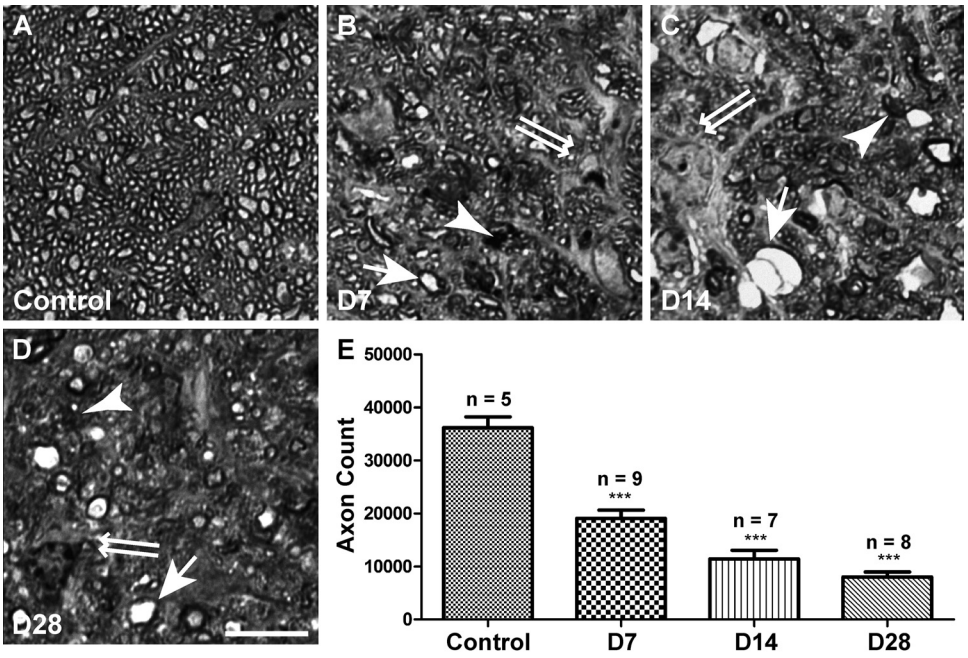

FIGURE 4. Axon degeneration in the myelinated optic nerve. (**A**–**D**) Representative images of PPD-stained optic nerve cross-sections. Samples were collected from control (**A**) and experimental animals 7 days (**B**), 14 days (**C**), and 28 days (**D**) after laser treatment. Healthy axons had robust and uniform myelin ensheathment surrounding a clear axoplasm (**A**). Degenerating axons were marked by darkly stained axoplasm or myelin debris (*arrowheads*). Axon swelling (*arrows*) and gliosis (*double arrows*) were also frequently observed in experimental samples. (**E**) Quantification of total axon count on PPD-labeled sections. The mean axon number was reduced 7 days after laser treatment and continued to decline at least until 28 days. Scale bar, 10 μm. $^{***}P < 0.001$.

axon damage, particularly around the ONH region, has been proposed to be a contributing factor for RGC death in glaucoma, we investigated how RGC axon integrity in this unmyelinated region may be influenced by laser treatment, especially at early time points. RGC axons were visualized using antibodies against the β-III subunit of tubulin and neurofilament (NF), two key structural components of the axon cytoskeleton. Although the axon labeling pattern using the two antibodies were similar, neurofilament labeling using SMI312 antibody resulted in visualization of the finer axonal processes with greater detail and was used to obtain higher magnification images.

The mouse ONH can be subdivided into the pre-lamina (at the level of retina) and lamina (at the level of sclera) regions.[27] We used different methodologies to best visualize the morphologies and trajectories of axons within these two regions. Longitudinal cryostat sections subjected to antibody staining (Fig. 5) were used to identify axonal changes within the lamina region (Fig. 5A, dotted bracket), whereas retinal whole-mounts (Fig. 6) were used to obtain the best visualization of the

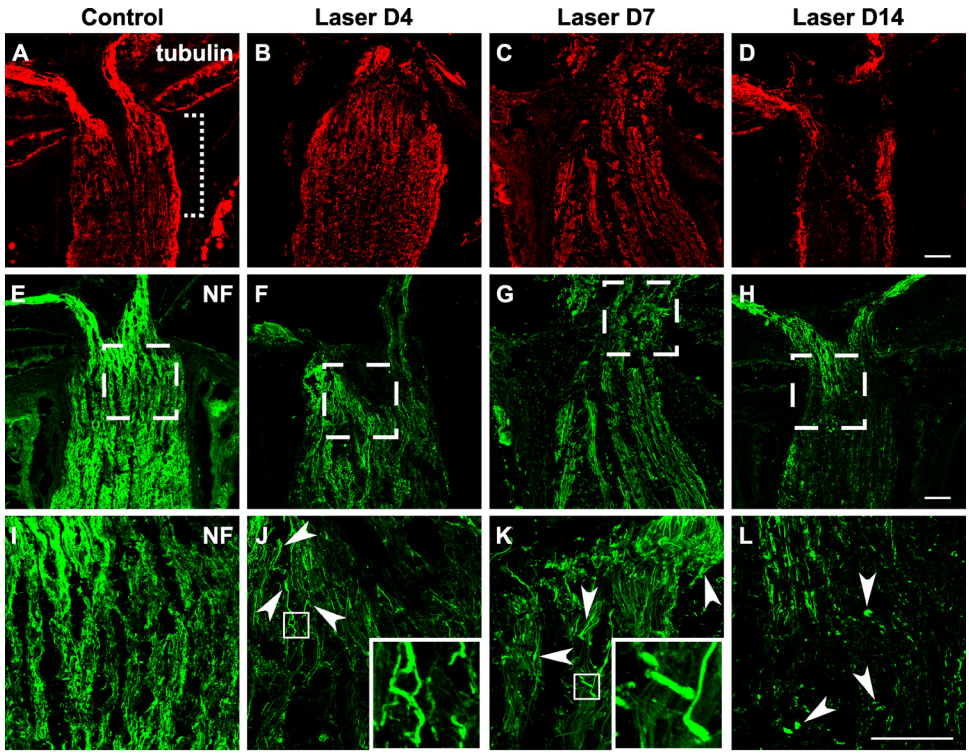

FIGURE 5. Early occurrence of axonal damage in the lamina ONH after laser treatment. Longitudinal cryosections through the ONH were immunostained for tubulin (**A**–**D**, *red*) and neurofilament (**E**–**L**, *green*). The retina is oriented toward the top of each image, and the optic nerve is oriented toward the bottom. (**A**, *dotted bracket*) Location of lamina ONH. (**I**–**L**) Boxed regions in (**E**–**H**). The uniform staining pattern and parallel organization of axons seen in controls (**A**, **E**, **I**) were disrupted in laser-treated eyes (**B**–**D**, **F**–**H**, **J**–**L**). Pathologic changes were observed as early as 4 days (**B**, **F**, **J**) after treatment and became more prevalent after 1 week (**C**, **G**, **K**). Axonal damage was initially manifested as localized enlargement (**J**, **K**, *arrowheads*) and undulating axon trajectory, examples of which are shown in the *insets*. The 2-week time point was marked by a loss of cytoskeletal immunoreactivity (**D**, **H**, **L**). Once-continuous axonal profiles were replaced with punctate degenerative debris (**L**, *arrowheads*) and regions devoid of axonal staining. Scale bar (**D**, **H**, **L**), 50 μm. For tubulin staining, between three and eight animals were examined at each time point; for NF staining, between three and eleven animals were examined.

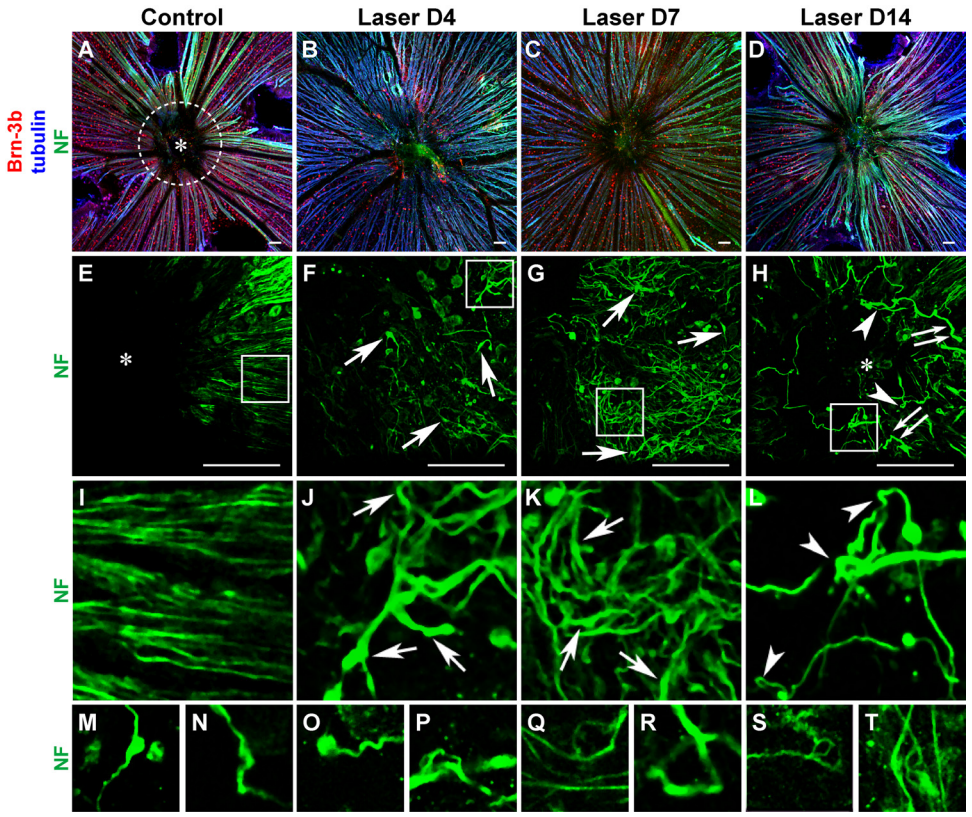

FIGURE 6. Aberrant axon trajectories at the pre-lamina ONH after laser treatment. Low-magnification images (**A–D**) of retinal whole-mounts immunolabeled with Brn-3b, tubulin and NF are presented to aid orientation and to correlate density of Brn-3b$^+$ RGCs with axon pathology. (**A**, *dotted white circle*) Location of pre-lamina ONH. Defasciculation and localized enlargements (*arrows*) were observed on axons as early as 4 days after laser treatment (**F**, **J**), and continued to become more pronounced at 1 week (**G**, **K**). The meandering trajectories of aberrant axons (most apparent in **J**, **K**) appeared in stark contrast to the radial organization of RGC axons in control retina (**E**, **I**). At 2 weeks, numerous axons were observed to be disconnected and terminated in retraction bulbs (**H**, *double arrows*). The aberrant trajectories were heterogeneous and complex and included twists, turns, and 180° loops (**H**, **L**, *arrowheads*). Ectopic axons were found at the center (*asterisk*) of the pre-lamina ONH (**H**), which was devoid of axonal staining in controls (**E**). A gallery exemplifies aberrant axon trajectories in additional retinal samples (**M–T**). Scale bar (**D–H**), 50 μm. $n = 5$ retinas for D4; $n > 20$ retinas for other time points.

morphology and trajectories of RGC axons in the pre-lamina region (Fig. 6A, white circle). The morphologic changes detected in the lamina and the pre-lamina regions, though similar in the first several days after laser treatment, became qualitatively different over the next 1 to 2 weeks.

Early Occurrence of Axon Degeneration in the Lamina ONH after Laser Treatment

In the control optic nerve lamina region, anti-tubulin and anti-NF immunostaining were uniform along the RGC axons (Figs. 5A, 5E, 5I). In contrast, in laser-treated eyes as early as 4 days after treatment, we observed a small number of axons at the lamina ONH region with localized enlargements (Fig. 5J, arrowheads and inset). Over the next few days, the overall staining pattern displayed more heterogeneity, with some axon segments showing intense immunoreactivity interrupted by patchy diminution of signal, consistent with a structural alteration in RGC axons (Fig. 5K). The axonal bundles normally aligned in parallel in this region also became distorted and undulating. By 2 weeks, the loss of cytoskeletal immunostaining was more widespread (Figs. 5D, 5H, 5L), reflecting a loss of intact axons. Concurrently, many small immunoreactive puncta were seen surrounding RGC axons, likely reflecting degenerated debris (Fig. 5L, arrowheads).

Aberrant Axon Trajectories at the Pre-Lamina ONH

In control retinal whole-mounts, tightly packed axon bundles converged onto the ONH in an orderly radial fashion (Figs. 6E, 6I). Four days after laser treatment, focal enlargements appeared on axons in the pre-lamina ONH region (Figs. 6F, 6J, arrows), similar to those observed in the lamina ONH (Fig. 5). Of note, axonal changes in the pre-laminar region, unlike that found in the lamina also included defasciculation of axon bundles (Fig. 6J), with individual axons exhibiting aberrant turning trajectories, giving them the appearance of frayed ends of ropes. At 1 week, more axons exhibited enlargements (Figs. 6G, 6K, arrows), defasciculation, and meandering trajectories (Fig. 6K). The normal radially directed axon trajectories seen converging at the optic disc was instead replaced by a more randomly directed pattern. By 2 weeks, RGC axons that appeared to be disconnected from their distal portions and terminating in bulbous endings were frequently observed (Fig. 6H, double arrows). In addition, numerous axons exhibited tortuous terminal segment trajectories, including axon twisting, turning, and even 180° axon loops (Figs. 6H, 6L, arrowheads). More examples of axons with aberrant trajectories are presented in Figures 6M–T. Although axons in control eyes were not found in the central portion of the pre-lamina ONH (asterisk, Figs. 6A, 6E), aberrantly projecting axons were readily observed in the same region in laser-treated eyes (asterisk, Fig. 6H). These morphologic changes and abnormal trajectories of RGC axons were similar to those encountered in glaucomatous eyes of DBA/2J mice (CTF, DS, unpublished observation, 2008).

This analysis using antibody staining of axon cytoskeletal elements and confocal microscopy revealed that the earliest detectable signs of alterations in RGC axonal integrity and trajectory occurred approximately 4 days after treatment. Although the lamina and pre-lamina regions demonstrated no significant difference at this early time point, by 2 weeks the morphology of axons within these two regions appeared remarkably distinct. The lamina region was marked by axonal degeneration and buildup of debris. On the other hand, the pre-lamina region was characterized by aberrant axon trajectories, exemplified by twisting and looping. Such complex trajectories observed here were reminiscent of the sprouting and reactive plasticity of adult axons proximal to localized trau-

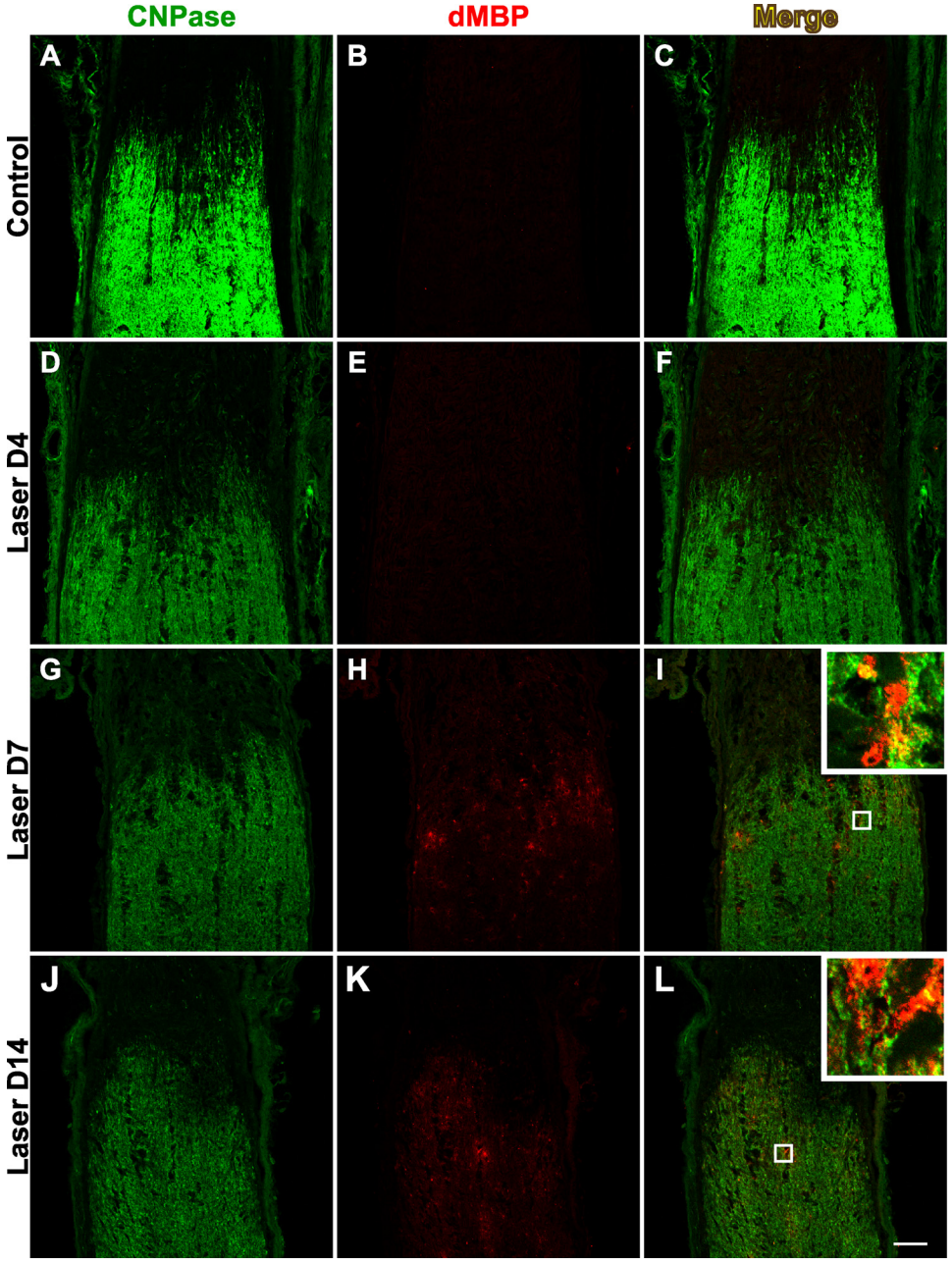

FIGURE 7. Detection of dMBP in the optic nerve. Oligodendrocytes were labeled with the CNPase marker (**A**, **D**, **G**, **J**), and dMBP served as an indicator of myelin damage (**B**, **E**, **H**, **K**). In the control optic nerves (**B**) and those harvested 4 days (**E**) after laser treatment, no specific immunoreactivity of dMBP was detected. At day 7, dMBP appeared primarily along the border of myelinated optic nerve with the unmyelinated ONH (**H**). After 2 weeks, the presence of dMBP could be identified further distal into the optic nerve (**K**). Merged images of CNPase and dMBP labeling are shown in (**C**, **F**, **I**, **L**), with the *insets* highlighting examples of both earlier stages of myelin degeneration characterized by colocalization of dMBP (*red*) and CNPase (*green*) in oligodendrocytes and later stages of myelin degeneration often characterized by the presence of dMBP alone. Scale bar, 50 μm. $n = 3$ sets of experiments.

matic injury in the mouse optic nerve[28] and elsewhere in the CNS.[29–32] Our findings were thus consistent with a model in which an early insult to RGC axons occurs at the lamina ONH causing axon structural breakdown, followed by an initiation of a reactive plasticity-like response in the remaining axon proximal segment in the pre-lamina region. The early signs of axonal pathology (days 4–7) occurred when RGC somas within the retina were still relatively preserved, as shown by Brn-3b labeling (Figs. 6B, 6C), and preceded the decrease in Brn-3b$^+$ RGC density that began approximately 1 to 2 weeks after laser treatment (Fig. 3).

Degeneration of Optic Nerve Myelin

Although axonal demyelination often results secondarily from CNS axon injury,[33] demyelinating diseases such as multiple sclerosis can also be the cause of axonal degeneration.[34] A recent study of laser-induced ocular hypertension in pigmented mice suggested that oligodendrocyte loss might precede significant RGC death.[8] Here we examined myelin damage in the optic nerve after LIOH in CD-1 mice and the chronology of this event in relation to axonal injury. To detect early signs of myelin degeneration, we took advantage of the fact that the degradation of myelin basic protein unmasks an epitope (dMBP) that can be detected by a specific antibody, thus allowing identification of injured white matter.[35,36] In control optic nerves, the presence of myelin was clearly demarcated after immunolabeling of mature oligodendrocytes by CNPase (2′,3′-cyclic nucleotide 3′-phosphodiesterase) antibody (Fig. 7A). As expected, there was no detectable signal after immunolabeling of dMBP (Fig. 7B). Similarly, in optic nerves from laser-treated eyes, dMBP was also not detectable in the first few days after treatment (Fig. 7E). However, beginning at 7 days after laser treatment, dMBP could be readily identified and occurred primarily along the border of the myelinated region with the unmyelinated ONH (Fig. 7H). At 2 weeks after laser treatment, dMBP was detected further distal into the optic

nerve (Fig. 7K). Higher magnification images (Figs. 7I, 7L, insets) demonstrated that the majority of dMBP immunoreactivity colocalized with cytoplasmic CNPase staining, confirming these degraded proteins were indeed of oligodendrocyte origin. Conversely, some dMBP immunoreactive structures were not found to overlap with CNPase, possibly reflecting oligodendrocyte processes in later stages of degeneration that have lost CNPase expression. Based on the earliest time of detection, alterations in RGC axon cytoskeletal structure at the ONH appeared to precede MBP degradation in the adjacent myelinated optic nerve.

Discussion

We demonstrated that IOP elevation can be induced in albino CD-1 mice by laser photocoagulation. Specific damage to RGC somas and RGC axons were observed, whereas other retinal layers were not significantly affected, consistent with the characteristic pathology of glaucoma. By taking advantage of the defined induction of IOP elevation, we placed a number of important pathologic changes in CD-1 LIOH in a rough temporal sequence. Our results demonstrated that the earliest detected morphologic changes in RGC axons occurred at the ONH by day 4 and consisted of localized axonal enlargements and undulating axon trajectories, followed progressively over the next 2 weeks by the accumulation of axonal debris in the lamina region and aberrant axon trajectories in the pre-lamina region. These early signs of ONH axonal damage substantially preceded evidence of myelin injury (beginning at 7 days) and RGC degeneration (at approximately 2 weeks), as manifested by the downregulation of Brn-3b and/or death of Brn-3b$^+$ cells within the retina.

Selective RGC Damage after LIOH in CD-1 Mice

The hallmark of glaucomatous disease is the selective damage to and loss of RGCs, with relative sparing of other retinal cell types. Several lines of evidence from the present study support the notion that LIOH in CD-1 mice triggers a similar pattern of RGC loss. Brn-3b staining of whole-mounted retina indicated the loss of immunoreactive cells over 4 weeks, suggesting progressive degeneration of RGCs. Histologic examination of sagittal retinal sections revealed a 33% reduction of cell density in the GCL, where RGC cell bodies reside. In addition, morphometric analysis showed that the thicknesses of other retinal layers were not affected, arguing against global ischemia. Axon degeneration characteristic of glaucomatous injuries also occurred, as demonstrated by axon counting in PPD-stained optic nerve.

Comparison with Other Animal Models of Glaucoma

Although monkeys[37,38] and rats[39–42] have been successfully induced to develop glaucoma, mouse models afford the additional advantages of cost-effectiveness and amenability for genetic manipulation. To date, a number of experimental glaucoma models have been reported in mice, including laser photocoagulation[8–11] and episcleral vein cauterization.[43] Compared with these models, LIOH in albino CD-1 offers potential advantages in terms of the accelerated time course and pronounced RGC damage. One study in C57BL/6 mice reported 28% RGC loss at 2 weeks,[8] but another in NIH Black Swiss mice demonstrated 63% axon loss at 12 weeks.[44] In contrast, CD-1 mice exhibited a 42% reduction of Brn-3b$^+$ RGCs at 2 weeks and a 78% reduction of myelinated axons at 4 weeks after LIOH.

It should be noted that because Brn-3b is downregulated in glaucomatous retinas,[26,45] the loss of Brn-3b immunoreactivity alone cannot be concluded as RGC loss. Instead, recent studies[26,45] interpret the reduction of RGC gene expression as a sign of degeneration, which is expected to mark a disease state preceding cell death itself. In the present study, significant axon degeneration (47%) in the myelinated optic nerve had already occurred 1 week after laser treatment, when the loss of Brn-3b$^+$ RGC somas was not yet prevalent. This observation agrees with previous reports that axon injury preceded RGC soma death.[25–27,45] At 2 weeks, both RGC axon and soma counts were significantly diminished (68% and 42%, respectively). By 4 weeks, axon number was reduced by 78%, whereas linear cell density in the GCL was reduced by only 33%. This may appear inconsistent at first glance; however, a substantial proportion of surviving cells in the GCL is expected to be displaced amacrine cells. Assuming amacrine cells accounted for 40% to 60% of the GCL cell population[18–21] and that they were not damaged by experimental glaucoma, the reduction of linear RGC density is estimated to be between 55% and 80% at 4 weeks. On the other hand, a 91% decrease of Brn-3b$^+$ cells was observed, possibly reflecting the downregulation of this protein in some surviving RGCs. In summary, by any of the three measures used in this study, the level of RGC injury induced by LIOH was clearly more severe in CD-1 mice than in pigmented mice.

Characteristics of IOP Elevation in CD-1 LIOH

Although the accelerated time course of RGC damage in CD-1 LIOH is advantageous in speeding up experimental analysis, it is necessary to bear in mind that this model is more acute than DBA/2J and human glaucoma and could potentially involve different underlying mechanisms. Although the disease present in DBA/2J mice models pigmentary glaucoma, CD-1 LIOH resulting from an acute blockage of fluid outflow may more closely resemble angle-closure glaucoma. Another major difference from existing published models is the transitory nature of IOP elevation in CD1 LIOH. IOP rose briefly from a baseline of 12 to 13 mm Hg to 27 to 29 mm Hg and returned to normal between 2 and 7 days after treatment. In our initial attempts at model development, we performed photocoagulation for a full 360° around the eye without avoiding the long posterior ciliary arteries. This treatment protocol typically resulted in acute IOP spikes of >70 mm Hg within 12 hours of laser treatment that could lead to ischemic changes and was thus abandoned. Translimbal laser treatment of 270° to 300° instead of 360° with the avoidance of long posterior ciliary arteries helped to eliminate acute pressure spikes after treatment. Repeated laser treatments to extend the period of IOP elevation were not consistently effective and frequently led to substantial additional ocular inflammation. The resultant corneal edema and scarring may then lead to false readings of elevated IOP. Although our laser treatment paradigm only resulted in a transient doubling of IOP for several days, this change in IOP in CD-1 mice was nevertheless sufficient to trigger highly reproducible morphologic changes in RGCs and their axons that mimic findings in glaucoma. Although IOP declined to baseline by 1 week, glaucomatous disease clearly progressed beyond that time point. This model, therefore, offers an opportunity to delineate pathophysiological mechanisms that can operate independently of sustained pressure elevation, which may have relevance to human cases with progressive worsening of glaucomatous disease despite IOP-lowering intervention.[46]

Axon Reactive Plasticity in the Pre-Lamina ONH

The aberrant looping trajectories of RGC axons in the pre-lamina ONH are strikingly reminiscent of the sprouting and reactive plasticity of adult RGC axons injured by optic nerve crush.[28] Although axonal sprouting has been described after

other CNS lesions[29,31,32] and in Alzheimer's disease,[47,48] aberrant growth of RGC axons in glaucomatous animals has not been previously appreciated. This RGC axon regrowth phenomenon may not be limited to mice; recent work in a rat laser-induced model of glaucoma has identified a similar phenomenon (Marsh-Armstrong N, personal communication, 2009). Axonal reactive plasticity in the pre-lamina region is most consistent with damage occurring more distally along the axons within the lamina region and agrees with previous reports in DBA/2J mice[26,27] identifying the lamina ONH as an initial site of glaucomatous injury. The ultimate fate of RGC axons that exhibit these aberrant trajectories is unknown, though their presence clearly demonstrates the ability of adult axons to maintain a limited growth/remodeling program. In the setting of glaucoma, it would be of interest to examine whether such axons exhibiting reactive plasticity are also present in human glaucomatous eyes and to identify the mechanisms underlying this form of plasticity.

Axonal Damage as an Early Manifestation of Disease

Because the onset of IOP elevation in LIOH is controlled by the investigator, this mouse model offers an opportunity to delineate the timing of some pathologic events that ultimately result in RGC loss. A finding from this study is the early onset of ONH axon degenerative changes and reactive plasticity after LIOH. Morphologic alterations of axons in the ONH preceded significant degeneration of myelin and RGC somas. These findings indicated that studies of the molecular nature of insults to RGC axons at the ONH and the intra-axonal response mechanisms may provide useful insight into disease. It is important to bear in mind that careful analysis of changes that may occur in the retina was not performed in the present study, and our results do not address the question whether there may also be early events that impact the dendritic and somatic compartments of RGCs that are either independent of, or related to RGC axonal changes occurring at the ONH. Nevertheless, the evidence of specific early RGC axon responses at the ONH indicates that the study of these events may be fruitful avenues for better understanding glaucoma pathophysiology. In addition, axonal responses to glaucomatous injury could serve as an early readout of the effectiveness of new therapeutic strategies.

Acknowledgments

The authors thank Jacque Duncan for use of the laser equipment and Ronald Hurd for technical advice on TonoLab (Colonial Medical Supply).

References

1. Levkovitch-Verbin H. Animal models of optic nerve diseases. *Eye.* 2004;18:1066–1074.
2. McKinnon SJ, Schlamp CL, Nickells RW. Mouse models of retinal ganglion cell death and glaucoma. *Exp Eye Res.* 2009;88:816–824.
3. Pang IH, Clark AF. Rodent models for glaucoma retinopathy and optic neuropathy. *J Glaucoma.* 2007;16:483–505.
4. Rasmussen CA, Kaufman PL. Primate glaucoma models. *J Glaucoma.* 2005;14:311–314.
5. Weinreb RN, Lindsey JD. The importance of models in glaucoma research. *J Glaucoma.* 2005;14:302–304.
6. Libby RT, Anderson MG, Pang IH, et al. Inherited glaucoma in DBA/2J mice: pertinent disease features for studying the neurodegeneration. *Vis Neurosci.* 2005;22:637–648.
7. Austad SN. Issues in the choice of genetic configuration for animal aging models. *Exp Gerontol.* 1997;32:55–63.
8. Nakazawa T, Nakazawa C, Matsubara A, et al. Tumor necrosis factor-alpha mediates oligodendrocyte death and delayed retinal ganglion cell loss in a mouse model of glaucoma. *J Neurosci.* 2006;26:12633–12641.
9. Aihara M, Lindsey JD, Weinreb RN. Experimental mouse ocular hypertension: establishment of the model. *Invest Ophthalmol Vis Sci.* 2003;44:4314–4320.
10. Gross RL, Ji J, Chang P, et al. A mouse model of elevated intraocular pressure: retina and optic nerve findings. *Trans Am Ophthalmol Soc.* 2003;101:163–169, discussion 169–171.
11. Grozdanic SD, Betts DM, Sakaguchi DS, Allbaugh RA, Kwon YH, Kardon RH. Laser-induced mouse model of chronic ocular hypertension. *Invest Ophthalmol Vis Sci.* 2003;44:4337–4346.
12. Savinova OV, Sugiyama F, Martin JE, et al. Intraocular pressure in genetically distinct mice: an update and strain survey. *BMC Genet.* 2001;2:12.
13. Du J, Tran T, Fu C, Sretavan DW. Upregulation of EphB2 and ephrin-B2 at the optic nerve head of DBA/2J glaucomatous mice coincides with axon loss. *Invest Ophthalmol Vis Sci.* 2007;48:5567–5581.
14. Libby RT, Li Y, Savinova OV, et al. Susceptibility to neurodegeneration in a glaucoma is modified by Bax gene dosage. *PLoS Genet.* 2005;1:17–26.
15. Leahy KM, Ornberg RL, Wang Y, et al. Quantitative ex vivo detection of rodent retinal ganglion cells by immunolabeling Brn-3b. *Exp Eye Res.* 2004;79:131–140.
16. Desai KH, Sato R, Schauble E, Barsh GS, Kobilka BK, Bernstein D. Cardiovascular indexes in the mouse at rest and with exercise: new tools to study models of cardiac disease. *Am J Physiol.* 1997;272:H1053–H1061.
17. Hayreh SS. The 1994 Von Sallman Lecture: the optic nerve head circulation in health and disease. *Exp Eye Res.* 1995;61:259–272.
18. Drager UC, Olsen JF. Ganglion cell distribution in the retina of the mouse. *Invest Ophthalmol Vis Sci.* 1981;20:285–293.
19. Jeon CJ, Strettoi E, Masland RH. The major cell populations of the mouse retina. *J Neurosci.* 1998;18:8936–8946.
20. Li Y, Schlamp CL, Nickells RW. Experimental induction of retinal ganglion cell death in adult mice. *Invest Ophthalmol Vis Sci.* 1999;40:1004–1008.
21. Li Y, Semaan SJ, Schlamp CL, Nickells RW. Dominant inheritance of retinal ganglion cell resistance to optic nerve crush in mice. *BMC Neurosci.* 2007;8:19.
22. Jakobs TC, Libby RT, Ben Y, John SW, Masland RH. Retinal ganglion cell degeneration is topological but not cell type specific in DBA/2J mice. *J Cell Biol.* 2005;171:313–325.
23. Kielczewski JL, Pease ME, Quigley HA. The effect of experimental glaucoma and optic nerve transection on amacrine cells in the rat retina. *Invest Ophthalmol Vis Sci.* 2005;46:3188–3196.
24. Xiang M, Zhou L, Peng YW, Eddy RL, Shows TB, Nathans J. Brn-3b: a POU domain gene expressed in a subset of retinal ganglion cells. *Neuron.* 1993;11:689–701.
25. Schlamp CL, Li Y, Dietz JA, Janssen KT, Nickells RW. Progressive ganglion cell loss and optic nerve degeneration in DBA/2J mice is variable and asymmetric. *BMC Neurosci.* 2006;7:66.
26. Soto I, Oglesby E, Buckingham BP, et al. Retinal ganglion cells downregulate gene expression and lose their axons within the optic nerve head in a mouse glaucoma model. *J Neurosci.* 2008;28:548–561.
27. Howell GR, Libby RT, Jakobs TC, et al. Axons of retinal ganglion cells are insulted in the optic nerve early in DBA/2J glaucoma. *J Cell Biol.* 2007;179:1523–1537.
28. Liu X, Hawkes E, Ishimaru T, Tran T, Sretavan DW. EphB3: an endogenous mediator of adult axonal plasticity and regrowth after CNS injury. *J Neurosci.* 2006;26:3087–3101.
29. Buckmaster PS, Zhang GF, Yamawaki R. Axon sprouting in a model of temporal lobe epilepsy creates a predominantly excitatory feedback circuit. *J Neurosci.* 2002;22:6650–6658.
30. Cajal R. *Degeneration and Regeneration of the Nervous System.* London: Oxford University Press; 1928.
31. Chuckowree JA, Dickson TC, Vickers JC. Intrinsic regenerative ability of mature CNS neurons. *Neuroscientist.* 2004;10:280–285.
32. Dancause N, Barbay S, Frost SB, et al. Extensive cortical rewiring after brain injury. *J Neurosci.* 2005;25:10167–10179.

33. Fitch MT, Silver J. CNS injury, glial scars, and inflammation: inhibitory extracellular matrices and regeneration failure. *Exp Neurol.* 2008;209:294–301.
34. Waxman SG. Axonal conduction and injury in multiple sclerosis: the role of sodium channels. *Nat Rev Neurosci.* 2006;7:932–941.
35. Li S, Stys PK. Mechanisms of ionotropic glutamate receptor-mediated excitotoxicity in isolated spinal cord white matter. *J Neurosci.* 2000;20:1190–1198.
36. Matsuo A, Lee GC, Terai K, et al. Unmasking of an unusual myelin basic protein epitope during the process of myelin degeneration in humans: a potential mechanism for the generation of autoantigens. *Am J Pathol.* 1997;150:1253–1266.
37. Weber AJ, Zelenak D. Experimental glaucoma in the primate induced by latex microspheres. *J Neurosci Methods.* 2001;111:39–48.
38. Quigley HA, Hohman RM. Laser energy levels for trabecular meshwork damage in the primate eye. *Invest Ophthalmol Vis Sci.* 1983;24:1305–1307.
39. Morrison JC, Moore CG, Deppmeier LM, Gold BG, Meshul CK, Johnson EC. A rat model of chronic pressure-induced optic nerve damage. *Exp Eye Res.* 1997;64:85–96.
40. Shareef SR, Garcia-Valenzuela E, Salierno A, Walsh J, Sharma SC. Chronic ocular hypertension following episcleral venous occlusion in rats. *Exp Eye Res.* 1995;61:379–382.
41. Levkovitch-Verbin H, Quigley HA, Martin KR, Valenta D, Baumrind LA, Pease ME. Translimbal laser photocoagulation to the trabecular meshwork as a model of glaucoma in rats. *Invest Ophthalmol Vis Sci.* 2002;43:402–410.
42. Yu S, Tanabe T, Yoshimura N. A rat model of glaucoma induced by episcleral vein ligation. *Exp Eye Res.* 2006;83:758–770.
43. Ruiz-Ederra J, Verkman AS. Mouse model of sustained elevation in intraocular pressure produced by episcleral vein occlusion. *Exp Eye Res.* 2006;82:879–884.
44. Mabuchi F, Aihara M, Mackey MR, Lindsey JD, Weinreb RN. Optic nerve damage in experimental mouse ocular hypertension. *Invest Ophthalmol Vis Sci.* 2003;44:4321–4330.
45. Buckingham BP, Inman DM, Lambert W, et al. Progressive ganglion cell degeneration precedes neuronal loss in a mouse model of glaucoma. *J Neurosci.* 2008;28:2735–2744.
46. Levin LA. Retinal ganglion cells and neuroprotection for glaucoma. *Surv Ophthalmol.* 2003;48(suppl 1):S21–S24.
47. Masliah E, Mallory M, Hansen L, et al. Patterns of aberrant sprouting in Alzheimer's disease. *Neuron.* 1991;6:729–739.
48. Phinney AL, Deller T, Stalder M, et al. Cerebral amyloid induces aberrant axonal sprouting and ectopic terminal formation in amyloid precursor protein transgenic mice. *J Neurosci.* 1999;19:8552–8559.